Unmodified Portable Telescope
for Space-to-Ground Optical Links

Gustav M. Pettersson*, Josep Perdigues, and Zoran Sodnik
European Space Agency – ESTEC, Noordwijk, the Netherlands
gupet@mit.edu, {josep.maria.perdigues.armengol, zoran.sodnik}@esa.int

Abstract—By providing high bandwidth with low power and size, optical communications have received intense interest in space applications. Inter-satellite links are now in everyday service with the European Data Relay System (EDRS), and several competent optical laser terminals for satellites have been constructed. The space-to-ground segment is challenged by atmospheric disturbances, and local weather necessitates site diversity. Fixed observatory-class or containerised ground stations have been demonstrated with favourable results, however, these are expensive to deploy in numbers. An alternative is to base the ground stations on commercial off-the-shelf (COTS) portable telescopes; easily deployable at low cost. We present the lowest cost ground station yet, below 10,000 euros or dollars, with only COTS components and requiring no modifications. In the Portable Optical Ground Station (POGS) described herein, a compact fine-tracking and fibre-coupling assembly replaces the telescope's eyepiece, and an external camera is added for automatic telescope Earth alignment and satellite acquisition. We demonstrate tracking performance at arcsecond-level accuracy and effective coupling into multi-mode fibres. POGS only requires low-resolution 256 by 256 pixel cameras, enabling expansion into short-wave infrared at low cost. All software and plans required to build the system are released as the free and open-source project *pypogs*, allowing our results to be immediately deployed.

I. Introduction

High bandwidth communication with low size and mass requirements have motivated decades of work in optical communication. Moving from radio to optical wavelengths allows small beam divergence with practical transmitter dimensions, hence more of the transmitted signal may be collected. The narrow optical beam further provides spatial selectivity which guarantees there is no interference with other links and avoids telecommunication regulations and licensing [1]. Strict pointing requirements and mobile satellite platforms necessitate active control of both transmitter and receiver to mitigate alignment losses. In 2001, the European Space Agency (ESA) Semiconductor Inter-satellite Link EXperiment (SILEX) established the first in-space optical link at $50\,\mathrm{Mb/s}$, with mutual acquisition and tracking between a low Earth orbit (LEO) and geostationary orbit (GEO) satellite [2]. Since 2016, the ESA European Data Relay System (EDRS) provides $1.8\,\mathrm{Gb/s}$ LEO-to-GEO optical links as part of the operational downlink for the European Union's Earth observation programme (Copernicus Sentinel 1 and 2) [3].

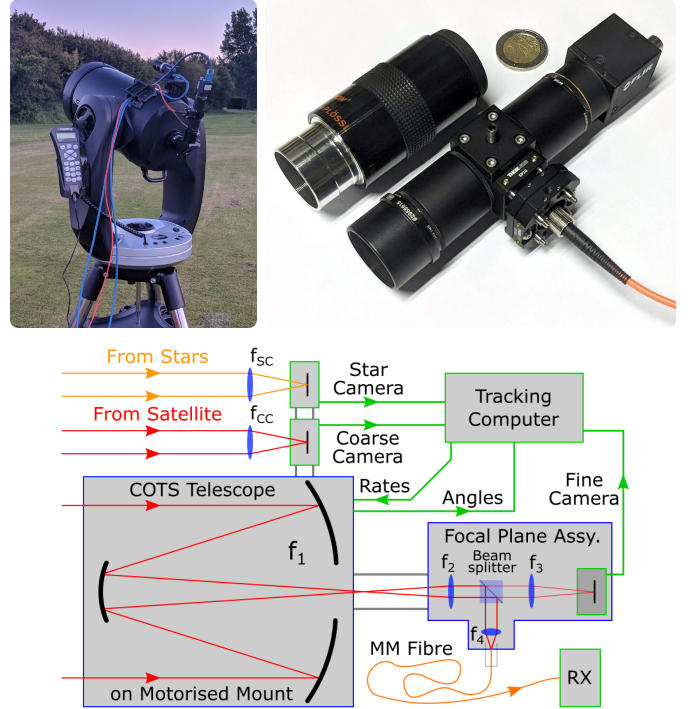*Now with the Massachusetts Institute of Technology, Cambridge, MA.

Fig. 1. POGS hardware and architecture. *Top-left:* Deployed system at sunset. *Top-right:* The FPA incorporating a fine camera and fibre coupling system; the standard eyepiece and a coin are shown for scale. *Bottom:* System diagram; in the test system the star and coarse camera are the same physical device.

Space-to-ground links are challenged by local atmospheric effects and weather. For large receiver apertures, the atmospherically distorted wavefront causes a focused image spot to move erratically, blur, and distort into speckles. Several mitigation techniques have been proposed for this [4], with adaptive optics (AO) [5] to measure and correct the wavefront emerging as the dominant technique. An alternative approach is to use one, or an array of, smaller receiver apertures to limit the atmospheric influence and reduce the complexity of each receiver [6]. Weather determines the availability of ground stations, necessitating the development of a diverse network of sites at good locations for reliable communication [7].

In this work, we introduce the Portable Optical Ground Station (POGS), in Fig. 1, for space-to-ground optical communications at the lowest cost yet, less than €10 000, by integrating a traditional optical architecture in a Focal Plane Assembly (FPA) which replaces the telescope's eyepiece. The

POGS includes automatic Earth alignment, arcsecond-level closed-loop satellite tracking, and coupling into a multi-mode (MM) fibre, exclusively made with commercial off-the-shelf (COTS) components without modifications or manufacturing. Furthermore, we release the software described herein and instructions on how to construct and use the system as a free and open-source project, *pypogs* (the PYthon POGS), available at *www.github.com/esa/pypogs*. This enables most computerised portable telescopes in the 20–50 cm class to automatically acquire, track, and couple a satellite's optical signal into a fibre for further use; providing a practical solution to the rising demand for diverse optical ground station networks and individual low-cost ground stations.

A. Related work

Several observatory-class optical ground stations have been constructed, e.g. the 1 m ESA Optical Ground Station (OGS) [8]. The OGS has demonstrated many receiver technologies and has been upgraded with AO to compensate for atmospheric effects [9]. The primary ground station for the Lunar Laser Communication Demonstration (LLDC) was the 4×40 cm NASA/MIT Lincoln Lab Lunar Lasercom Ground Terminal (LLGT), which demonstrated the use of four smaller receive telescopes to limit atmospheric effects, individually coupled into MM fibres with electronically combined signals [10]. A mobile ground station was demonstrated with the 60 cm DLR Transportable Optical Ground Station (TOGS) by folding into a truck for transport [11]. The container-based 26 cm DLR Transportable Adaptive Optical Ground Station (TAOGS) further demonstrated AO capability and coupling into single-mode fibres in a movable ground station [12].

Portable optical ground stations, transported and deployed by a single person, were demonstrated with the MIT Portable Telescope for Lasercom (PorTeL) [13]. PorTeL was based on a 28 cm low-cost COTS portable telescope modified with an optical breadboard affixed to the rear of the telescope, mounting a fine steering mirror (FSM), tracking camera, and photodetector. A star camera was attached externally and methods were developed for automatic Earth alignment [14] and closed-loop tracking. Tracking errors for LEO satellites illuminated by the sun of $1.9''$–$4.9''$ (arcseconds) root mean square (RMS) were demonstrated [15]. In this work, we use a similar telescope as PorTeL and demonstrate equivalent performance. However, improved tracking methods allow the FSM and all modifications to be eliminated, further reducing the cost and effort required to deploy the system.

B. Testing considerations

For practicality, this work is conducted in the visible spectrum ($\lambda \approx 0.5\,\mu$m) with a small $D = 20$ cm telescope. Noting that diffraction and atmospheric effects scale by λ/D [16] and $D/r_0 \propto D/\lambda^{6/5}$ [17] (where r_0 is the Fried parameter) respectively, our results are comparable to a $D = 40$ cm telescope operating in near-infrared ($\lambda \approx 1\,\mu$m).

Without a cooperating satellite, the available practical targets, i.e. LEO satellites illuminated by the sun and stars, are

Item	Cost (€ or $)
COTS portable telescope, 20–50 cm	$2000 - 5000$
Accessories (battery, camera mount, etc.)	500
Two (visible/NIR) tracking cameras	2×500
Coarse camera lens	500
Focal Plane Assembly including optics	1000
Tracking computer	1000
Total	$6000 - 9000$

relatively dim and broadband optics must be used. Assuming a typical target is of second apparent magnitude ($4.0\,\text{nW/m}^2$ bolometric irradiance [18]; i.e. the brightness of *Polaris*), the irradiance is $1.3\,\text{nW/m}^2$ before atmospheric losses if the entire visible spectrum ($1/3$ of total power) is captured. For comparison, the EDRS downlink has been measured at 1–$2\,\mu\text{W/m}^2$ [19], and the NODE (LEO CubeSat at 1000 km) downlink budget predicts a ground irradiance of $28\,\text{nW/m}^2$ [20]. Compared to our testing, the high power monochromatic downlinks used for communication will provide better signal-to-noise ratio and improved optical performance.

Several optical communication architectures use short-wave infrared (SWIR) wavelengths (e.g. 1550 nm) which may not be detected with standard Silicon cameras. Low-cost SWIR (e.g. InGaAs) cameras provide a relatively low resolution of 320×256 px. We therefore set the read-out window of our coarse and fine tracking cameras to 256×256 px to show that such cameras are sufficient for the POGS.

II. SYSTEM DESIGN

The POGS architecture is motivated in this section and the specifics of our test setup are given in Section II-C. Fig. 1 shows the system and Table I provides a cost estimate.

A. Tracking

The satellite is tracked with a COTS portable telescope (focal length f_1) with two motorised perpendicular axes (in this work referred to as altitude and azimuth, but holds in general), by sending desired angular rates from a tracking computer. The telescope aperture D is chosen to limit atmospheric effects to image motion and blurring without breaking into speckles. Depending on wavelength and local conditions this is 20–50 cm. A fine camera detects the position of the target satellite and dictates the mount rates to keep the downlink signal entering the fibre. With atmospheric effects limited, the image on the fine camera is approximately Gaussian and therefore optimal spot localisation (centroiding) will be attained with a fine camera plate scale of half the spot-size. Due to increased noise, denser sampling than half the spot diameter degrades the localisation performance [21]. At good to average sites the spot size due to seeing is expected to be at best 1–$2''$, therefore a fine camera plate scale of 0.5–$1\,''/\text{px}$ gives optimal performance, with better than $0.1''$ localisation readily attained. The fine camera and fibre are mounted with the FPA to any telescope via the standard 1.25 inch or 2 inch eyepiece barrel connector. With lenses f_2, f_3, and f_4 in the

FPA the effective fibre-to-sky focal length $f_{\mathrm{MMF}} = f_1/f_2 \cdot f_4$ and fine camera focal length $f_{\mathrm{FC}} = f_1/f_2 \cdot f_3$ are individually optimised. The numerical aperture (NA) limits the largest angle which may enter a fibre and therefore the shortest usable focal length as: $f_{\mathrm{MMF}} \geq D/(2\mathrm{NA})$. For a standard fibre (NA $= 0.22$) and a $D = 40\,\mathrm{cm}$ telescope we should have $f_{\mathrm{MMF}} \approx 1000\,\mathrm{mm}$. The fibre core size is determined to give a sufficient field of view (FOV) on the sky to guarantee stable coupling. A 50–$200\,\mu\mathrm{m}$ core diameter is typically required depending on mount performance and satellite orbit.

B. Acquisition

A two-step process initially acquires and tracks the target satellite onto the fine camera. First, an externally mounted star camera with a lens (f_{SC}) is fixed to the telescope tube to find the telescope's Earth alignment and mount calibration without user input, based on star patterns. The target satellite's orbit is propagated and the telescope pointed accordingly. A wide FOV coarse camera with a lens (f_{CC}) is also externally mounted to the telescope tube and acquires the satellite despite position or timing uncertainty, upon which the pointing direction is corrected to bring the downlink into the FPA. The star and coarse camera may be the same physical device, however, if e.g. a spectral filter is used to block background light to the coarse camera, these must be two separate devices to allow the star camera to capture dim stars.

Satellite orbits are obtained from the U.S. Space Command's *Space-Track* service (*www.space-track.org*) in a Two-Line Element (TLE) format. The uncertainty of these orbital elements and time synchronisation error in the tracking computer may lead to the target satellite appearing far away from its predicted position in the sky. Therefore, the required FOV of the coarse camera to guarantee acquisition must be found. Worst-case observation angle errors for some interesting orbits are presented in Table II, showing that a coarse camera FOV of $2.8°$ is required for some LEO satellites. However, if LEO satellites will not be tracked, or accurate satellite position data and time is available, the proposed architecture may be simplified by omitting the coarse camera.

C. Test system

The test system consists of a $D = 20\,\mathrm{cm}$, $f_1 = 2000\,\mathrm{mm}$ telescope on an altitude-azimuth mount [CPC800, Celestron, USA]. Achromatic lenses $f_2 = 25\,\mathrm{mm}$, $f_3 = 30\,\mathrm{mm}$, $f_4 = 10\,\mathrm{mm}$ and a 90:10 (R:T) non-polarising beam-splitter are used in the FPA [Thorlabs, USA], giving $f_{\mathrm{FC}} = 2400\,\mathrm{mm}$ and $f_{\mathrm{MMF}} = 800\,\mathrm{mm}$. USB3 connected cameras [BFS-U3-31S4M-C, FLIR IIS, Canada] with $6.9\,\mu\mathrm{m}$ pixels (after 2×2 binning) are used with a read-out region of $1024\,\mathrm{px}\times768\,\mathrm{px}$ for the star camera, and $256\,\mathrm{px}\times256\,\mathrm{px}$ for the coarse and fine cameras. The same physical device is used as star and coarse camera with a $f_{\mathrm{SC}} = f_{\mathrm{CC}} = 35\,\mathrm{mm}$, lens [HF35XA-5M, Fujinon, Japan]. The plate scale and FOV for each camera is:

- Star camera: $40.6''/\mathrm{px}$, $11.5°\times8.7°$
- Coarse camera: $40.6''/\mathrm{px}$, $2.9°\times2.9°$
- Fine camera: $0.6''/\mathrm{px}$, $154''\times154''$

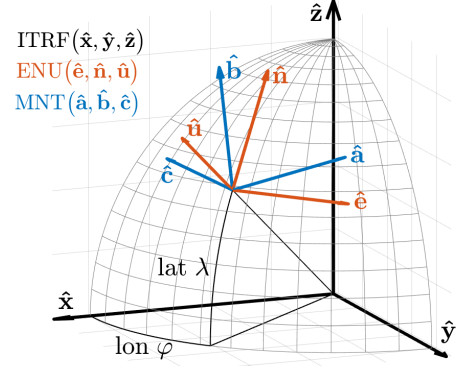| Orbit (circular)	Pos. σ	Ang. 3σ	Ang. vel.	Total
450 km (LEO)	2.34 km	$0.89°$	$0.97\,°/\mathrm{s}$	$1.4°$
650 km (LEO)	0.37 km	$350''$	$0.66\,°/\mathrm{s}$	$0.4°$
20 000 km (MEO)	0.16 km	$5.0''$	$\approx 40\,''/\mathrm{s}$	$25''$
36 000 km (GEO)	0.57 km	$9.8''$	≈ 0	$10''$

Fig. 2. Basis vectors for ITRF, ENU, and MNT on an octant section of Earth.

III. TRACKING METHODS

A. Coordinate frames

The orientation of the telescope and the relative direction from the telescope to the target must be known in some mutual coordinate frame to point the telescope towards the target. Since the telescope is Earth-fixed (when deployed), and the target is mobile, it is natural to choose an Earth-fixed coordinate frame. Calculating the relative target direction involves considerable complications due to the motion of Earth. We bypass these by using the popular open-source software packages *Astropy* [24] and *Skyfield* [25] to provide relative target directions, $\hat{\mathbf{v}}$, to stars and planets, and Earth-orbiting satellites respectively, in the standard Earth-centred Earth-fixed International Terrestrial Reference Frame (ITRF).

Traditionally, a telescope's orientation is ensured to coincide with the local tangential east north up (ENU) coordinate frame whereby the mount altitude (alt; also called elevation) and azimuth (az) angles directly correspond to the angle above the horizon and angle away from north (towards east) respectively. At latitude λ and longitude φ on Earth, the ENU basis vectors are, expressed in ITRF, see Fig. 2:

$$\hat{\mathbf{e}}_{\mathrm{ITRF}}(\lambda, \varphi) = \begin{bmatrix} -\sin\lambda, & \cos\lambda, & 0 \end{bmatrix}^{\mathrm{T}}$$
$$\hat{\mathbf{n}}_{\mathrm{ITRF}}(\lambda, \varphi) = \begin{bmatrix} -\cos\lambda\sin\varphi, & -\sin\lambda\sin\varphi, & \cos\varphi \end{bmatrix}^{\mathrm{T}}$$
$$\hat{\mathbf{u}}_{\mathrm{ITRF}}(\lambda, \varphi) = \begin{bmatrix} \cos\lambda\cos\varphi, & \sin\lambda\cos\varphi, & \sin\varphi \end{bmatrix}^{\mathrm{T}}$$
$$(1)$$

($\cdot^{\mathrm{T}}$ denotes transpose) and converting the relative target direction $\hat{\mathbf{v}}$ from ITRF to ENU is a simple change of basis:

$$\hat{\mathbf{v}}_{\mathrm{ENU}} = \begin{bmatrix} \hat{\mathbf{e}}_{\mathrm{ITRF}} & \hat{\mathbf{n}}_{\mathrm{ITRF}} & \hat{\mathbf{u}}_{\mathrm{ITRF}} \end{bmatrix}^{\mathrm{T}} \hat{\mathbf{v}}_{\mathrm{ITRF}} \qquad (2)$$

Let $\hat{\mathbf{v}}_{\mathrm{ENU}}=[e, n, u]^{\mathrm{T}}$, then the required ENU alt and az angles are defined by:

$$\mathrm{alt}_{\mathrm{ENU}} = \arcsin(u) \tag{3}$$
$$\mathrm{az}_{\mathrm{ENU}} = \arctan 2(e, n)$$

For a portable system, it is undesirable to force the user to physically align the telescope to Earth. Therefore, we introduce the mount local coordinate frame MNT, and a method for automatically finding it (see Section III-C), where a basis of three orthonormal vectors $\{\hat{\mathbf{a}}, \hat{\mathbf{b}}, \hat{\mathbf{c}}\}$ are chosen based on the (unconstrained and location-independent) orientation of the telescope when it is deployed. $\hat{\mathbf{c}}$ is chosen to be the az rotation axis (pointing up), $\hat{\mathbf{a}}$ is chosen to be the alt rotation axis (pointing right as seen from behind), and $\hat{\mathbf{b}}$ is chosen to complete a right-handed set. With this choice, the MNT and ENU bases will coincide for a telescope which is aligned traditionally. Converting the relative target direction from ITRF to MNT alt and az angles is thus equivalent to (2) and (3) with $\{\hat{\mathbf{e}}, \hat{\mathbf{n}}, \hat{\mathbf{u}}\}$ replaced by $\{\hat{\mathbf{a}}, \hat{\mathbf{b}}, \hat{\mathbf{c}}\}$. The desired MNT alt and az angles and rates (by numerical differentiation) are calculated in real-time; no pre-planning of passes is necessary.

B. Mount corrections

With an ideal telescope, the commanded angles sent to the mount directly correspond to MNT alt and az angles. However, in practice, a mount correction model must be introduced to reach the full potential of the telescope mount. We therefore introduce three pointing corrections, 1) alt_0: alt angle encoder offset; 2) C_D: alt deflection coefficient; 3) C_P: alt-az non-perpendicularity; which are also automatically found by the procedure in Section III-C, and define the commanded coordinates (COM) as:

$$\mathrm{alt}_{\mathrm{COM}} = (1 + C_D)\,\mathrm{alt}_{\mathrm{MNT}} + \mathrm{alt}_0 \tag{4}$$
$$\mathrm{az}_{\mathrm{COM}} = \mathrm{az}_{\mathrm{MNT}} - C_P \tan(\mathrm{alt}_{\mathrm{MNT}}) \tag{5}$$

which are the angles sent to the mount to physically point the telescope to the desired MNT direction. The choice of the MNT $\hat{\mathbf{a}}$ axis precludes an azimuth encoder offset. The pointing model here is equivalent to the one proposed in [14], with simplified formulation.

The star camera pointing is used as the system reference, with small angle offsets added for any pointing discrepancies between the star, coarse, and fine cameras.

C. Auto-alignment

The telescope orientation, $\{\hat{\mathbf{a}}, \hat{\mathbf{b}}, \hat{\mathbf{c}}\}$, and mount corrections, $\{\mathrm{alt}_0, C_D, C_P\}$ are found analytically by capturing the ITRF orientation of the telescope at eight pairs of COM alt and az angles distributed across the sky. For each star camera observation, the right ascension and declination are found by a method based on [26]. These are converted to an ITRF vector with *Astropy* using the image time-stamp. Only three observations are necessary to solve for the MNT frame and corrective terms. Eight observations are used to provide four independent estimates of each term, providing direct statistical alignment assessment and redundancy.
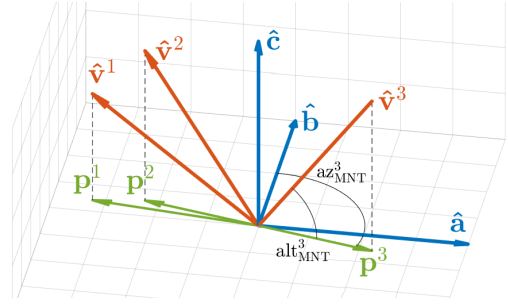

Fig. 3. Three auto-alignment observations $\hat{\mathbf{v}}^k$ from the star camera give the MNT basis vectors $\hat{\mathbf{a}}$, $\hat{\mathbf{b}}$, and $\hat{\mathbf{c}}$ from the procedure in Section III-C.

Given three observations $k = 1, 2, 3$ at commanded positions $\mathrm{alt}_{\mathrm{COM}}^k$ and $\mathrm{az}_{\mathrm{COM}}^k$ with respective measured pointing vectors $\hat{\mathbf{v}}_{\mathrm{ITRF}}^k$, and with the constraints:

$$\mathrm{alt}_{\mathrm{COM}}^1 \neq \mathrm{alt}_{\mathrm{COM}}^2 = \mathrm{alt}_{\mathrm{COM}}^3 \tag{6}$$
$$\mathrm{az}_{\mathrm{COM}}^1 = \mathrm{az}_{\mathrm{COM}}^2 = \mathrm{az}_{\mathrm{COM}}^3 + 180° \tag{7}$$

the MNT basis, and mount corrective terms are analytically solved for with this procedure. The subscript ITRF is dropped from all vectors in this section and the procedure is illustrated in Fig. 3. Proceed as follows:

1) For the constraints of observations 2 and 3, (4) and (5) give $\mathrm{alt}_{\mathrm{MNT}}^2 = \mathrm{alt}_{\mathrm{MNT}}^3$ and $\mathrm{az}_{\mathrm{MNT}}^2 = \mathrm{az}_{\mathrm{MNT}}^3 + 180°$. Accordingly, the MNT azimuth rotation axis is:

$$\hat{\mathbf{c}} = (\hat{\mathbf{v}}^2 + \hat{\mathbf{v}}^3) / \|\hat{\mathbf{v}}^2 + \hat{\mathbf{v}}^3\| \tag{8}$$

2) The MNT altitude is by definition:

$$\mathrm{alt}_{\mathrm{MNT}}^k = 90° - \arccos(\hat{\mathbf{v}}^k \cdot \hat{\mathbf{c}}) \tag{9}$$

3) The altitude deflection is therefore, from (4), and $\mathrm{alt}_{\mathrm{COM}}^1 \neq \mathrm{alt}_{\mathrm{COM}}^2$ giving $\mathrm{alt}_{\mathrm{MNT}}^1 \neq \mathrm{alt}_{\mathrm{MNT}}^2$:

$$C_D = \frac{\mathrm{alt}_{\mathrm{COM}}^2 - \mathrm{alt}_{\mathrm{COM}}^1}{\mathrm{alt}_{\mathrm{MNT}}^2 - \mathrm{alt}_{\mathrm{MNT}}^1} - 1 \tag{10}$$

4) The encoder offset is found by averaging, from (4):

$$\mathrm{alt}_0 = \frac{1}{3} \sum_{k=1}^{3} \left(\mathrm{alt}_{\mathrm{COM}}^k - (1 + C_D)\mathrm{alt}_{\mathrm{MNT}}^k \right) \tag{11}$$

5) The axes non-perpendicularity is, by projecting the measured vectors into the plane normal to $\hat{\mathbf{c}}$, and (5):

$$\hat{\mathbf{p}}^k = (\hat{\mathbf{v}}^k - (\hat{\mathbf{v}}^k \cdot \hat{\mathbf{c}})\hat{\mathbf{c}}) / \|\hat{\mathbf{v}}^k - (\hat{\mathbf{v}}^k \cdot \hat{\mathbf{c}})\hat{\mathbf{c}}\|$$

$$C_P = \frac{\mathrm{az}_{\mathrm{MNT}}^1 - \mathrm{az}_{\mathrm{MNT}}^2}{\tan(\mathrm{alt}_{\mathrm{MNT}}^1) - \tan(\mathrm{alt}_{\mathrm{MNT}}^2)} \tag{12}$$

$$= \frac{\arcsin((\hat{\mathbf{p}}^1 \times \hat{\mathbf{p}}^2) \cdot \hat{\mathbf{c}})}{\tan(\mathrm{alt}_{\mathrm{MNT}}^1) - \tan(\mathrm{alt}_{\mathrm{MNT}}^2)}$$

6) The MNT azimuth is therefore, from (5):

$$\mathrm{az}_{\mathrm{MNT}}^k = \mathrm{az}_{\mathrm{COM}}^k + C_P \tan(\mathrm{alt}_{\mathrm{MNT}}^k) \tag{13}$$

7) The second basis vector is defined to coincide with $\text{alt}_{\text{MNT}} = \text{az}_{\text{MNT}} = 0$ by rotating the projected vectors:

$$\mathbf{b} = \sum_{k=1}^{3} \left(\hat{\mathbf{p}}^k \cos\left(\text{az}_{\text{MNT}}^k\right) + \left(\hat{\mathbf{c}} \times \hat{\mathbf{p}}^k\right) \sin\left(\text{az}_{\text{MNT}}^k\right) \right)$$

$$\hat{\mathbf{b}} = \mathbf{b}/\|\mathbf{b}\| \tag{14}$$

8) The third basis vector is chosen to complete the orthonormal right-handed set, by defining $\hat{\mathbf{a}} = \hat{\mathbf{b}} \times \hat{\mathbf{c}}$.

The observations are captured at $\text{alt}_{\text{COM}} \in \{40°, 60°\}$, and $\text{az}_{\text{COM}} \in \{-135°, -45°, 45°, 135°\}$. After star alignment, the pointing discrepancies of star, coarse, and fine cameras are automatically calibrated by tracking a bright star in a spiral pattern until it is detected on the fine camera, and the angular offsets are recorded.

D. Feedback control

As reported by Riesing [15, ch. 4], all previous closed-loop optical ground stations have implemented camera-based feedback controllers by incorporating the observed angular errors as offsets to the desired mount *angles*. Thus, at every update of the controller, instantaneous large mount rates (angular velocities) are commanded to remove the measured errors. In this work, we include the observed errors as offsets to the desired *rates* via a proportional-integral (PI) controller, providing smoothly varying control signals and therefore smaller residual errors than previous efforts.

For the two control axes alt_{MNT} and az_{MNT} we introduce a feedback term u to the rate commands sent to the mount.

$$\dot{\text{alt}}_{\text{COM}} = \dot{\text{alt}}_{\text{MNT,planned}} + u_{\text{alt}}$$

$$\dot{\text{az}}_{\text{COM}} = \dot{\text{az}}_{\text{MNT,planned}} + u_{\text{az}} \tag{15}$$

where $\dot{\text{alt}}_{\text{COM}} \approx \dot{\text{alt}}_{\text{MNT}}$ and $\dot{\text{az}}_{\text{COM}} \approx \dot{\text{az}}_{\text{MNT}}$ are implied by (4) and (5) respectively. u is updated at a frequency f by a PI controller with gains K_P and K_I, based on the measured error e for each update t:

$$u_{\text{alt}}^t = K_P \left(e_{\text{alt}}^t + \frac{1}{K_I} \sum_{i=0}^{t} \frac{e_{\text{alt}}^i}{f} \right)$$

$$u_{\text{az}}^t = K_P \left(e_{\text{az}}^t + \frac{1}{K_I} \sum_{i=0}^{t} \frac{e_{\text{az}}^i}{f} \right) \tag{16}$$

with standard methods for integral windup protection implemented. The units for K_P and K_I are hertz and seconds respectively. The error terms are provided by different sources depending on the controller mode. The basic mode is open-loop (OL), with the mount angle encoders as the source:

$$e_{\text{alt,OL}} = \text{alt}_{\text{MNT,planned}} - \text{alt}_{\text{MNT,encoder}}$$

$$e_{\text{az,OL}} = \text{az}_{\text{MNT,planned}} - \text{az}_{\text{MNT,encoder}} \tag{17}$$

where the MNT encoder angles are calculated by the inverse of (4) and (5) from the mount's reported COM encoder angles. Camera feedback is provided in modes coarse closed-loop (CCL) and fine closed-loop (FCL) using the coarse and fine camera respectively. For these modes, the error terms derive

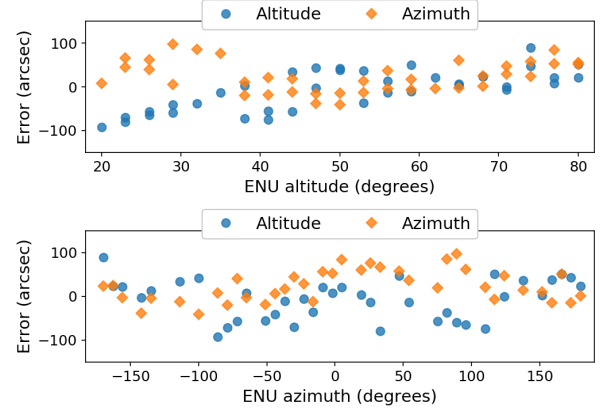| Parameter	Auto-calibrated value			Uncertainty
$\hat{\mathbf{a}}$	[−.1729	.9838	.0471]$^{\text{T}}$	—
$\hat{\mathbf{b}}$	[−.7692	−.1647	.6174]$^{\text{T}}$	18″
$\hat{\mathbf{c}}$	[.6151	.0705	.7853]$^{\text{T}}$	17″
alt_0	0.9843°			18″
C_P	0.1641°			20″
C_D	−0.465%			0.040%

Fig. 4. Measured open-loop pointing errors in alt (vertical) and az (horizontal).

from the satellite position (x, y) (increasing to the right and up respectively) measured on each camera:

$$e_{\text{alt,CCL}} = p_{\text{coarse}} \left(y_{\text{coarse}} - y_{0,\text{coarse}} \right)$$

$$e_{\text{az,CCL}} = \frac{p_{\text{coarse}} \left(x_{\text{coarse}} - x_{0,\text{coarse}} \right)}{\cos\left(\text{alt}_{\text{MNT,encoder}}\right)} \tag{18}$$

where p is the plate scale and (x_0, y_0) is the desired satellite position on the camera (e.g. the centre). The error for FCL is constructed identically. Background computational threads provide (x, y) at the control loop's request by continuously reading images and updating the position of the satellite on the respective camera.

The control mode is automatically switched between OL, CCL, and FCL by evaluating transition criteria based on the quality of the available coarse and fine camera tracks.

IV. RESULTS

A. Auto-alignment

The automatic alignment procedure completed in $3\,\text{min}\,15\,\text{s}$, including image acquisitiona and all computations. The result of one auto-alignment is provided in Table III. In clear-sky conditions, the procedure was successful at nautical twilight or later, typically with seven or eight star images solved.

To verify the accuracy of the alignment and the open-loop pointing performance of the telescope mount, an all-sky alignment test was conducted immediately after the alignment in Table III. The telescope was commanded to 42 positions evenly spaced in ENU alt and az and the star camera used to record the actual pointing direction. The resulting errors are shown in Fig. 4, with RMS pointing errors of $45.4''$ and $42.6''$ in the alt and az directions respectively.
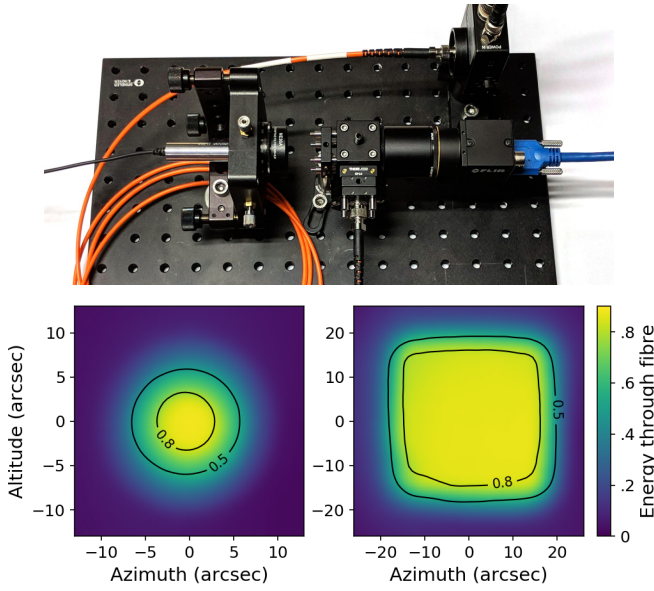
Fig. 5. *Top:* Laboratory setup for measuring FPA coupling efficiency. *Bottom:* Energy coupled with the FPA through a 50 μm round core fibre (left) and 150 μm square core fibre (right) at given on-sky angle. Maximum coupled energy is 88% and 87% respectively.

TABLE IV
GEOMETRICAL AND MEASURED FIBRE FOV AND MAXIMUM ALLOWED
TRACKING RMS ERROR TO COUPLE 80% ENERGY AT 3-SIGMA LEVEL.

Fibre	Geom. FOV	Meas. 80% FOV	Max. RMSE
50 μm	13″	6.5″	1.1″
150 μm	39″	31″	5.2″

B. Fibre coupling

Due to the dimness of stars and satellites illuminated by the sun, we were unable to measure the received power through the fibre in the field. Therefore, laboratory tests were performed where the fibre coupling was measured as a function of the alt and az angles, which is used in Section IV-C to predict the fibre coupling during tracking. Shown in Fig. 5, the collimating lens f_2 was removed from the FPA and a collimated 3 mm diameter, 1 μW, 635 nm laser mounted to a kinematic mount was used to simulate the received signal. An amplified photodiode measured the power at the end of the fibre as the laser was scanned in the alt and az directions and the centroid location was recorded with the fine camera. Two fibres were tested, one 50 μm NA=.22 round core and one 150 μm NA=.39 square core. The maximum allowable RMS error guaranteeing 80% coupling were calculated in Table IV to 1.1″ and 5.2″ respectively. This was reached approximately 12 μm (3″) in from the edge of the cores.

C. Tracking accuracy

To test tracking performance, LEO satellites and stars were tracked, with a typical example provided for each in this section. Automatic acquisition and mode switching were used.

For the LEO satellite *Terra*, in Fig. 6, FCL tracking was sustained over 6 min with 3″–5″ RMS tracking error. The satellite first appeared on the coarse camera (came out of Earth
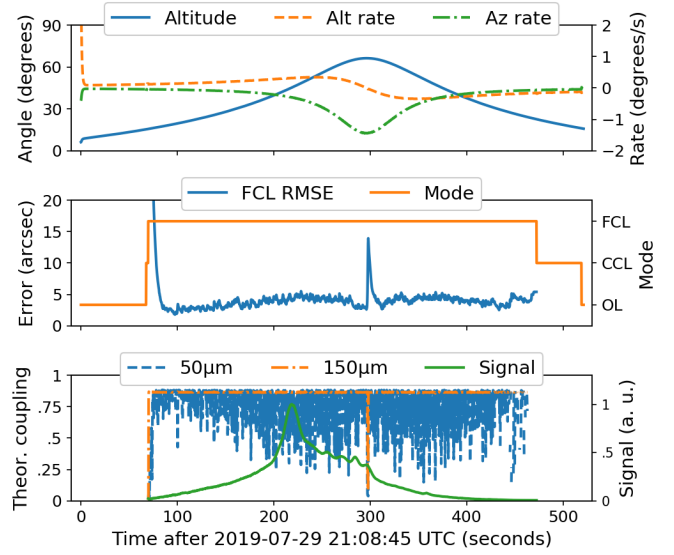

Fig. 6. Closed-loop tracking of the LEO satellite *Terra* (700 km orbit). *Top:* Telescope MNT altitude and COM rates. *Middle:* Exponential moving RMS error as measured on the fine camera, and the tracking mode. *Bottom:* Theoretical fibre coupling efficiency from the measurements of Fig. 5 for both tested fibres, and the received signal power measured on the fine camera.
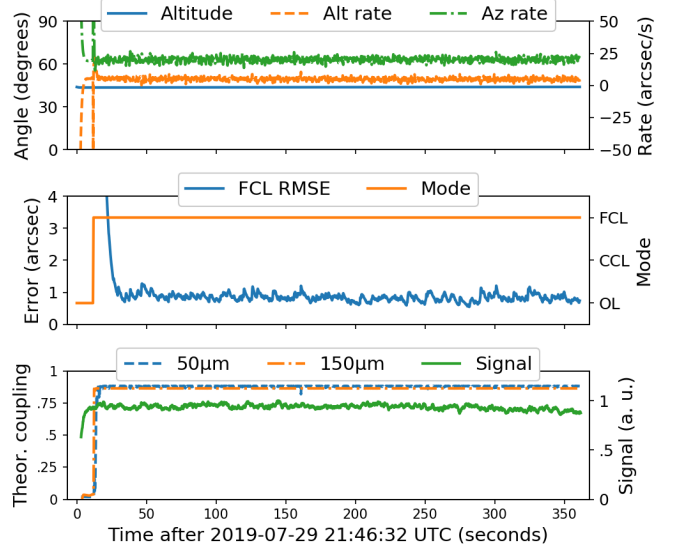

Fig. 7. Closed-loop tracking of the star *Altair* (declination +8.9°; rate 15″/s) as an analogue for satellites beyond LEO. Same views as in Fig. 6.
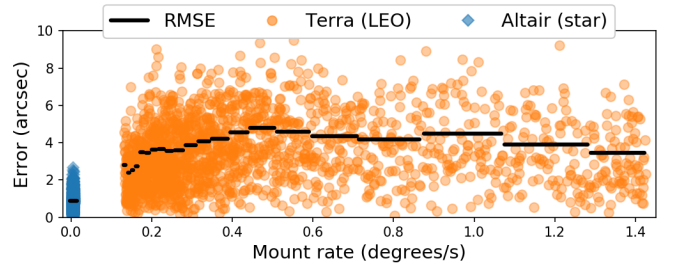

Fig. 8. Total tracking error as a function of the tracking rate for the data in Figs. 6 and 7. RMS error calculated per 100 samples (outliers excluded).

shadow) after $70\,$s. Upon this, the satellite was automatically acquired and confirmed, and the system transitioned from OL to CCL and subsequently from CCL to FCL, in less than $10\,$s. A stutter lasting $1\,$s was observed as the alt rate switched from positive to negative. The theoretical fibre coupling efficiency was calculated by looking up the measured coupling from Section IV-B for each error measurement on the fine camera. As predicted from Table IV, the theoretical coupling into the $150\,\mu$m core fibre was consistently high, with mean 86.5% and standard deviation (SD) 0.2% (excluding stutter). For the $50\,\mu$m fibre the mean coupling was 74% with SD 15%.

For the star *Altair*, in Fig. 7, stable $1''$ RMS error was observed during FCL tracking, with faster than $10\,$s transition to FCL after slewing to the target. The theoretical fibre coupling efficiency was calculated for the $150\,\mu$m core fibre to mean 86.5% with SD 0.02%, and for the $50\,\mu$m core fibre to mean 88.1% with SD 0.3%.

The relationship between mount tracking rate and RMS error in the preceding tracking data is explored in Fig. 8. The observed RMS error increased from $1''$ to $4''$ as the rate increased to $0.4\,°/$s, and thereafter settled.

V. DISCUSSION

With our methods, we demonstrated that it is possible to reach sufficient tracking performance for applications in space-to-ground optical communications with unmodified COTS portable telescopes. Smooth tracking errors without step-corrections, and randomly distributed alignment residuals, indicate that performance is limited by fundamental mount precision (encoders, backlash, flexure etc.). A minor low-altitude alignment error from atmospheric refraction is evident; correcting for this is straightforward, however, this would introduce undesirable location dependence.

Standard (50–$62.5\,\mu$m) MM fibres are used in this architecture for tracking satellites beyond LEO, and therefore a wide range of COTS fibre-coupled receivers can be directly used. For LEO satellites the required core size is larger (100–$200\,\mu$m) and an optomechanical assembly using a free-space photodetector is suggested. A typical $NA = .22$ fibre has an exit focal ratio small enough that a 2:1 or greater reduction in core size to photodetector is possible by collimating and refocusing the light exiting the fibre.

A ground station beacon is used in many architectures, especially for LEO-to-ground links, to assist the space terminal in quickly acquiring the ground station. This may be added to the proposed architecture by affixing a COTS fibre collimator externally (besides the coarse and star cameras) with a laser or light-emitting diode as the beacon light source.

Uplinking may be implemented as an independent telescope with the same architecture and tracking software presented here, with the signal launched into the fibre. If tracking is offset by the point-ahead angle, the need for a point-ahead mirror assembly is entirely removed. Spectral or polarisation filters in the FPA must be selected to isolate the uplink sufficiently that the downlink may still be tracked. Spectral filtering may also be used to enable daytime operations by blocking out the sky background.

REFERENCES

[1] H. Henniger and O. Wilfert, "An introduction to free-space optical communications." *Radioengineering*, vol. 19, no. 2, 2010.

[2] T. Tolker-Nielsen and G. Oppenhauser, "In-orbit test result of an operational optical intersatellite link between ARTEMIS and SPOT4, SILEX," in *Proc. SPIE 4635*, 2002.

[3] H. Hauschildt, S. Mezzasoma, H. L. Moeller, M. Witting, and J. Herrmann, "European data relay system goes global," in *Proc. IEEE Int. Conf. Space Optical Systems and Applications (ICSOS)*, 2017.

[4] Z. Sodnik and M. Sans, "Extending EDRS to laser communication from space to ground," in *Proc. IEEE Int. Conf. Space Optical Systems and Applications (ICSOS)*, 2012.

[5] J. M. Beckers, "Adaptive optics for astronomy: principles, performance, and applications," *Annu. Rev. Astron. Astrophys*, vol. 31, no. 1, 1993.

[6] J. Garnham, P. Shubert, and R. Pierson, "Low-cost optical communications ground terminal architecture for inter-planetary and high data rate communications links," in *Proc. SPIE 10524*, 2018.

[7] C. Fuchs and F. Moll, "Ground station network optimization for space-to-ground optical communication links," *IEEE/OSA J. Opt. Commun. Networking*, vol. 7, no. 12, 2015.

[8] R. H. Czichy, Z. Sodnik, and B. Furch, "Design of an optical ground station for in-orbit checkout of free-space laser communication payloads," in *Proc. SPIE 2381*, 1995.

[9] Z. Sodnik, J. P. Armengol, R. H. Czichy, and R. Meyer, "Adaptive optics and ESA's optical ground station," in *Proc. SPIE 7464*, 2009.

[10] M. E. Grein *et al.*, "Design of a ground-based optical receiver for the lunar laser communications demonstration," in *Proc. IEEE Int. Conf. Space Optical Systems and Applications (ICSOS)*, 2011.

[11] A. Shrestha and M. Brechtelsbauer, "Transportable optical ground station for high-speed free-space laser communication," in *Prroc. SPIE 8517*, 2012.

[12] E. Fischer *et al.*, "Development, integration and test of a transportable adaptive optical ground station," in *Proc. IEEE Int. Conf. Space Optical Systems and Applications (ICSOS)*, 2015.

[13] K. Riesing, H. Yoon, and K. Cahoy, "A portable optical ground station for low-earth orbit satellite communications," in *Proc. IEEE Int. Conf. Space Optical Systems and Applications (ICSOS)*, 2017.

[14] K. L. C. Kathleen M. Riesing, Hyosang Yoon, "Rapid telescope pointing calibration: a quaternion-based solution using low-cost hardware," *J. Astron. Telesc. Instrum. Syst.*, vol. 4, no. 3, 2018.

[15] K. M. Riesing, "Portable optical ground stations for satellite communication," Ph.D. dissertation, Massachusetts Institute of Technology, 2018.

[16] E. Abbe, "Beiträge zur Theorie des Mikroskops und der mikroskopischen Wahrnehmung," *Archiv für mikroskopische Anatomie*, vol. 9, no. 1, 1873.

[17] D. L. Fried, "Optical Resolution Through a Randomly Inhomogeneous Medium for Very Long and Very Short Exposures," *J. Opt. Soc. Am.*, vol. 56, no. 10, 1966.

[18] E. E. Mamajek *et al.*, "Resolution B2 on Recommended Zero Points for the Absolute and Apparent Bolometric Magnitude Scales," *IAU*, 2015.

[19] J. M. Perdigues *et al.*, "The ESA's optical ground station for the EDRS-A LCT in-orbit test campaign: upgrades and test results," in *Proc. Int. Conf. Space Optics (ICSO)*, 2017.

[20] E. Clements *et al.*, "Nanosatellite optical downlink experiment: design, simulation, and prototyping," *Opt. Eng.*, vol. 55, no. 11, 2016.

[21] R. E. Thompson, D. R. Larson, and W. W. Webb, "Precise Nanometer Localization Analysis for Individual Fluorescent Probes," *Biophysical J.*, vol. 82, no. 5, 2002.

[22] R. Wang, J. Liu, and Q. Zhang, "Propagation errors analysis of TLE data," *Adv. Space Res.*, vol. 43, no. 7, 2009.

[23] T. Flohrer, H. Krag, and H. Klinkrad, "Assessment and Categorization of TLE Orbit Errors for the US SSN Catalogue," in *Proc. Advanced Maui Optical and Space Surveillance Technologies Conf.*, 2008.

[24] The Astropy Collaboration *et al.*, "The Astropy Project: Building an Open-science Project and Status of the v2.0 Core Package," *Astron. J.*, vol. 156, no. 3, 2018.

[25] B. Rhodes, "Skyfield: Elegant Astronomy for Python." [Online]. Available: http://rhodesmill.org/skyfield/

[26] J. Brown, K. Stubis, and K. Cahoy, "TETRA: Star Identification with Hash Tables," in *Proc. AIAA/USU Conf. Small Satellites*, 2017.